3
Enhancement in Photo-electrochemical Properties

This chapter describes about optical absorption and photo electrochemical properties of pristine hematite and surface fluorinated hematite. The chapter is composed of five sections and eleven sub-sections. The introduction of chapter is described in section 3.1. The results and discussion of physical characterization techniques are expressed in the section 3.2. Optical characterization for bandgap measurement is discussed in section 3.3. The electrochemical characterization, working electrode preparation method and DSSC fabrication are presented in the section 3.4 and the section 3.5 covers concluding remarks.

3.1 INTRODUCTION

Hematite or α-Fe_2O_3 has attracted immense attention in the recent past as it is highly abundant, non-toxic and low cost material with a bandgap of 2.1–2.2 eV. However, certain drawbacks limits the use of α-Fe_2O_3 in solar application such as low mobility of carriers (<0.1 $cm^2V^{-1}s^{-1}$) [Morin, 1954] high recombination rates, short excited state lifetime (< 10 ps), [Cherepy et al., 1998] short diffusion length (2-4 nm), [Kennedy and Frese, 1978] poor light absorption, [Cesar et al., 2009] and improper band position [Goodenough, 1971] for unassisted water splitting. There is lot of impetus in improving its properties by structural modification, variation in morphology and by doping [Lian et al., 2009; Yilmaz and Unal, 2016].

In last few years, extrinsic fluorine anion doping of semiconducting metal oxides such as SnO_2, Co_3O_4, TiO_2 and Fe_2O_3 have emerged out as an important route for surface passivation that inhibits e^-/h^+ recombination and improves charge carriers lifetime. In addition to this, fluorine doping can result in tunable optical absorption and modified band position for enhancement in photo-electrochemical activity. Theoretical studies also anticipated that the replacement of O^{-2} by F^- can effectively reduce the electrical resistivity of Fe_2O_3 [Amatucci and Pereira, 2007]. For example, Tondello et al. synthesized F-doped Co_3O_4 by plasma enhanced chemical vapor deposition method using fluorinated β-diketonatecobalt derivative as a single fluorine and cobalt precursor and observed a significant improvement in hydrogen production. Similarly, Choi et al. carried out fluorination of TiO_2 using sodium fluoride for enhanced photo catalytic action [Kim and Choi, 2007; Park and Choi, 2004]. The enhancement in catalytic activity is understandable due to increase in Lewis acidity of Fe-centers by substitution of surface oxygen atoms with fluorine. For example, Lee et al. synthesized F, N-doped Fe_2O_3 using ammonium fluoride and urea and used it for super capacitor application [Karthikeyan et al., 2014]. Zhu et al. observed rapid photo catalytic degradation of R6G dye using fluorinated SnO_2 [Wang et al., 2015],[Gasparotto et al., 2011].

Several fluorine-doped metal oxides have been synthesized in order to enhance the electrochemical performance of energy storage devices. Among solution-based fluorinating agents, mainly HF and NH_4F are generally used however, these act preferentially as growth directing agent with no evidence for fluorination in the growth of metal oxides [Sophronov et al., 2016]. Herein F-TEDA was utilized as a fluorinating agent that gives electrophilic fluorine in solution as the reactive species. In this work, a facile yet effective hydrothermal strategy for the

in-situ preparation of surface F-Fe_2O_3 was developed by modifying the known method for dendritic growth of α-Fe_2O_3 [Cao et al., 2005]. Since, F-TEDA have never been attempted for fluorination of metal oxides before in literature, this study is fundamentally important for understanding the interaction and effect of fluorine with α-Fe_2O_3. The study is focused on the interplay between the fluorine content (varying F-TEDA concentration 0% to 40%) and resulting structural, optical and photo-electrochemical properties for application in visible light photo-catalysis and dye sensitized solar cells.

F-TEDA is a well-known, commercially available, stable fluorinating reagent that acts as a source of electrophilic fluorine in organic synthesis [Banks et al., 1996; Banks and Syvretb, 1992; Lal et al., 1996]. F-TEDA was utilized for fluorination of α-Fe_2O_3, an inorganic material, due to its high reactivity and ease of handling as compared to the other sources of fluorine such as HF, XeF_2 and F_2 [Hart and Syvret, 1999; Nyffeler et al., 2004]. Synthesis was scaled up in different-sized Teflon vessels of 100, 200 and 800 mL capacity. The hydrothermal reaction for $K_3[Fe(CN)_6]$ was carried out with and without F-TEDA at an optimized reaction condition of ~140°C for 48 hrs.

3.2 CHARACTERIZATION OF SURFACE FLUORINATED HEMATITE

The physical & chemical characterization of surface fluorinated hematite was carried out to obtain physical information and effects of fluorination. The physical properties of active materials are assessed by adopting different characterization techniques. These characterization data and their analysis are presented in sub-sections from 3.2.1 to 3.2.6 as following:

(3.2.1) *pH measurements* were performed for monitoring of reaction.
(3.2.2) *NMR* was recorded for surface fluorination reaction mechanism of hematite and F-TEDA.
(3.2.3) *SEM and TEM studies* express the surface morphology, geometrical shape and size of sample.
(3.2.4) *X-ray diffraction* and structural analysis are delivering information about crystal structure and phase formation.
(3.2.5) *XPS spectra* and analysis gives information about quantitative and qualitative elemental analysis.
(3.2.6) *Raman spectra* performed for iron and oxygen lines and their shifting with respect to fluorination.

3.2.1 pH Measurements

The pH changes in the reaction medium were monitored before and after reaction completion to gain better insight in the process of fluorination (Figure 3.1). The pH of the reaction mixture containing Fe precursor and F-TEDA (10 wt.% - 40 wt.%) is comparatively lower (pH = 3.4 - 4.0) than Fe precursor in water (pH = 6.2) as the F-TEDA is a salt of strong acid and weak base. However, after the hydrothermal reaction, pH of the supernatant becomes higher due to CN^- assisted dissociation of water that result in formation of OH^- ions [Green et al., 2017].

The overall reaction of fully hydrolyzed form of ferricyanide anion, fluorination and to form fluorinated hematite crystals is presented in equation 3.1. Subsequent dissociation of water is presented in equation 3.2.

$$[Fe(CN)_6]^{3-} \rightarrow FeOOH/Fe(OH)_3 + \text{F-TEDA} \rightarrow FeO(OH)_{1-x}F_x/Fe(OH)_{3-x}F_x \rightarrow \text{F-}\alpha\text{-}Fe_2O_3 \quad (3.1)$$

$$CN^- + H_2O \rightarrow HCN + OH^- \quad (3.2)$$

For higher concentrations of F-TEDA, the pH of supernatant after the reaction decreases gradually. As seen from Figure 3.1 (bottom curve), the overall pH change for the reaction is higher in presence of fluorinating agent (10, 20 and 30 wt. % of F-TEDA) as compared to pristine. With higher F-TEDA (40 wt.%), overall pH change after reaction is similar to pristine due to neutralization of hydroxide ions by excess of F-TEDA. Here, F-TEDA plays an important

role in influencing the pH of the reaction medium and thus the growth of Fe based nanostructures.

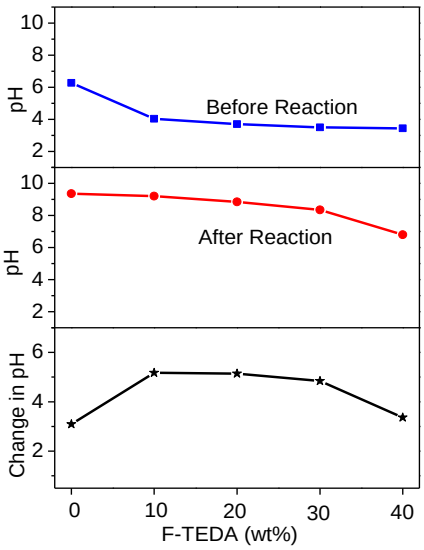

Figure 3.1: pH changes before and after reaction for increasing concentration of F-TEDA

3.2.2 NMR Studies

The complete mechanism of F-TEDA reaction with $K_3[Fe(CN)_6]$ under hydrothermal condition is difficult to explain. However, NMR studies were performed externally to verify the release of electrophilic F^+ in the reaction mixture. The NMR spectrum of F-TEDA shows a peak at +48.7 ppm corresponding to N–F bond (F^+ species) and doublet at −150.3 and −150.8 ppm (two BF_4 anion) as shown in Figure 3.2a. After the reaction, the peak at +48.7 ppm corresponding to the F^+ species disappears while the doublet from BF_4 anion at ~150 ppm shifts to 119.2 ppm due to the change in environment of BF_4 anions after the liberation of F^+ from F-TEDA during the hydrothermal reaction (Figure 3.2b).

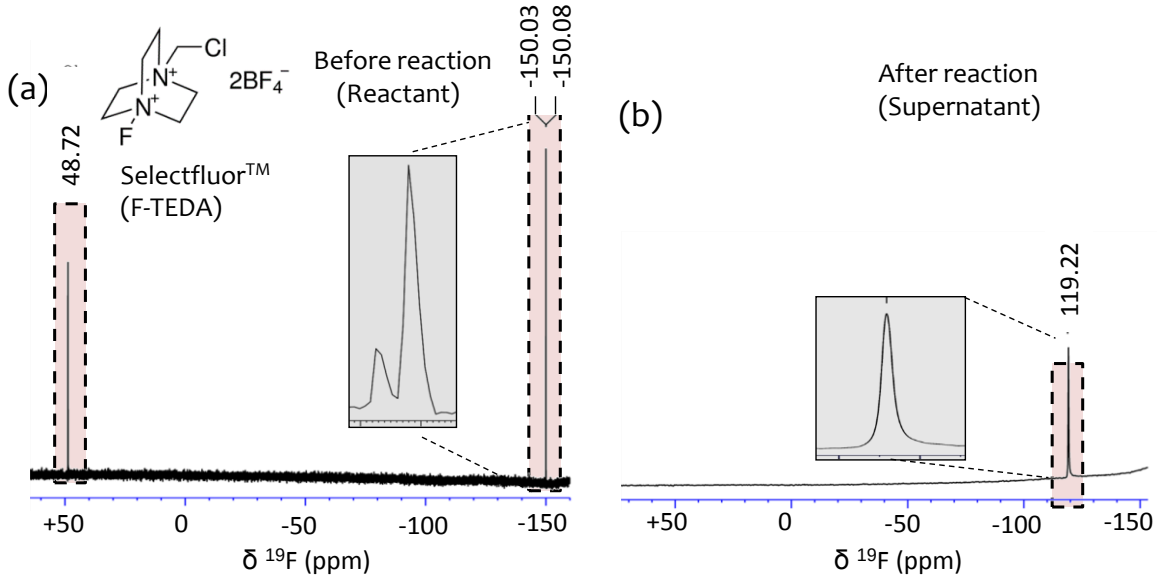

Figure 3.2: F-19 NMR spectra of the reaction medium, (a) before and (b) after reaction (from supernatant)

3.2.3 SEM and TEM Studies

The pristine and F-Fe_2O_3 synthesized under identical growth conditions were characterized by FESEM and TEM imaging (Figure 3.3). The pristine α-Fe_2O_3 has a typical dendrite type structure (Figure 3.3a and 3.3f) with the backbone oriented in $[1\bar{1}00]$ direction. The surface and structure of α-Fe_2O_3 undergoes modification by systematic introduction of F-TEDA in the reaction mixture. At 10% F-TEDA, some of the dendrite structure starts assembling along four directions (Figure 3.3b and 3.3g). When 20% F-TEDA was added to the reaction mixture, α-Fe_2O_3 exhibited a clear change in shape from single dendrite to snow flake-type nanostructure with six-fold symmetry (Figure 3.3c and 3.3h). At much higher F-TEDA concentration (30% or more), the growth rate is accelerated in all crystallographic directions resulting in loose aggregates of nanoparticles (Figure 3.3d, 3.3e, 3.3i and 3.3j). Beyond 40% F-TEDA concentration, the morphology of F- α-Fe_2O_3 loses uniformity and becomes random.

The α-Fe_2O_3 synthesized with 20% of F-TEDA was further examined in detail. The electron diffraction pattern with zone axis [0001] shows the hexagonal reciprocal lattice of the corresponding snowflake like structure. The inter-planar distance was measured to 0.2528 nm corresponds to the $\{11\bar{2}0\}$ family of planes growing in $[1\bar{1}00]$ family direction. The EDS maps of Fe-Kα, O-Kα and F-Kα corresponding to the TEM images in Figure 3.3(m-o) exhibit uniformly distributed signals indicating that fluorine is uniformly covering the surface of α- Fe_2O_3.

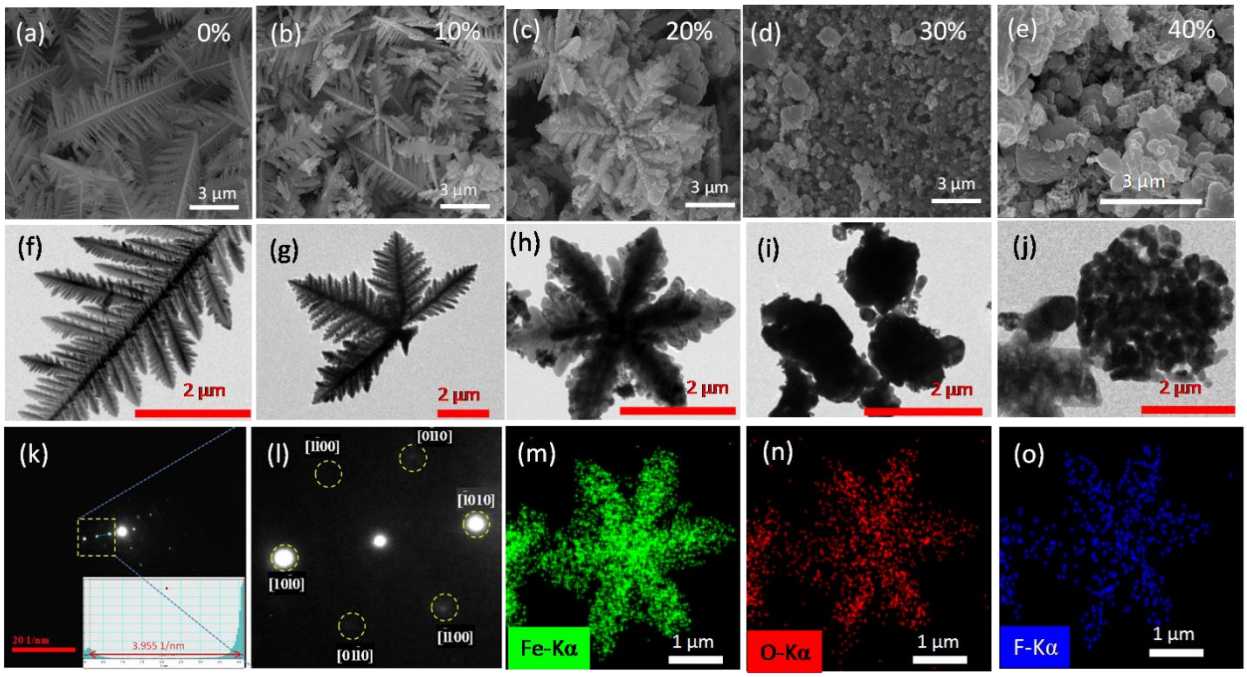

Figure 3.3: (a-e) FESEM images and corresponding (f-j) TEM images of pristine and F-Fe_2O_3 with 10%, 20%, 30% and 40% of F-TEDA respectively. (k,l) SAED pattern at low and high magnification and (m-o) EDS imaging of F-Fe_2O_3 with 20% F-TEDA

3.2.4 X-ray Diffraction Studies

The phase, crystallinity and orientation of α-Fe_2O_3 before and after fluorination (0 -40% F-TEDA, with 10% wt. increment) were examined by powder X-ray diffraction (Figure 3.4a). All the peaks in the XRD pattern for pristine as well as F-Fe_2O_3 matches with JCPDS 33-0664 card number of hematite. This indicates that there is no change in the phase or composition and it is only surface fluorination. The intense and broad peaks are marked of nanocrystalline nature of α-Fe_2O_3. Neither new peaks nor any shift in position of peaks could be observed upon fluorination of α-Fe_2O_3 since F^- has a similar ionic radius (133 pm) with that of O^{-2} (140 pm), therefore F-Fe_2O_3 has lower lattice distortion.[Wang et al., 2017] The average crystallite size was ~35.6 nm, calculated from highest intense peak using Scherrer equation. The crystallite size of F-Fe_2O_3 was similar to average crystallite size of the pristine α-Fe_2O_3 (Table 3.1).

Table 3.1: Calculation of crystallite size (nm) of pristine and F-Fe_2O_3using Scherrer equation with respect to (104) and (110) planes

F-TEDA (wt %)	*(104)*	*(110)*
0	35.6	43.4
10	34.0	34.9
20	36.7	40.8
30	32.2	36.6
40	35.7	37.2

It can be observed that with increase in F-TEDA concentration used for fluorination of α-Fe_2O_3, there is a linear increase in growth along [110] direction as seen by the increase in (110) diffraction peak with respect to (104) peak intensity (Figure 3.4b). The (110) orientation of α-Fe_2O_3 is known to possess anisotropic conductivity much higher than (104) orientation due to closed-packing (inset, Figure 3.4b) resulting in improved charge collection of photo-excited charge carrier [Cai et al., 2016; Iordanova et al., 2005; Nakau, 1960]. Therefore, the F-Fe_2O_3 is expected to have better potential for water splitting.

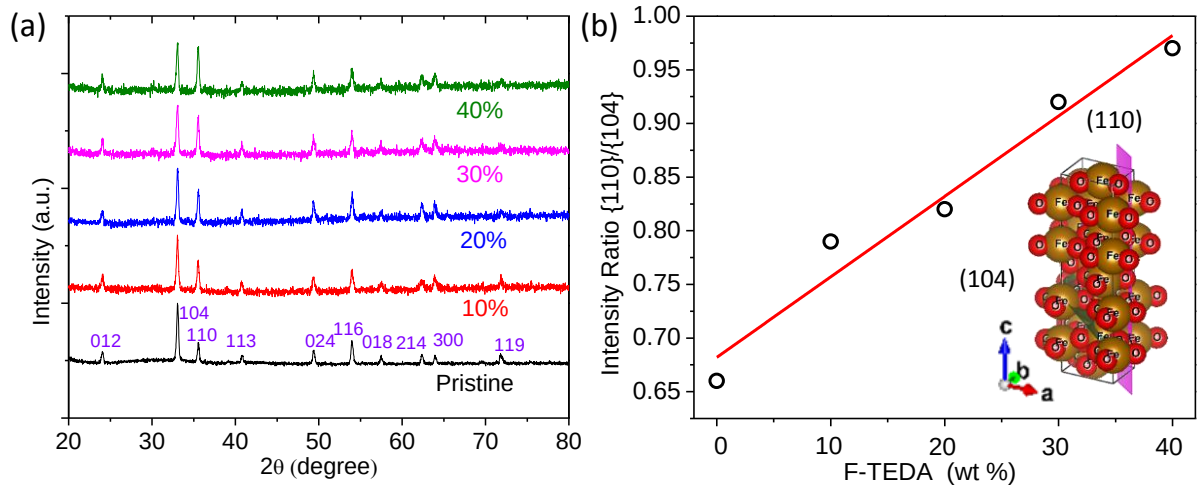

Figure 3.4: (a) XRD patterns. (b) Variation in intensity of {110/104} peak ratio with respect to weight% of F-TEDA. Inset shows the packing of atoms in both (110) and (104) crystallographic planes

Fluorinated hematite samples prepared using 50%, 60% and 70%wt. of F-TEDA in reaction medium was also analyzed for phase and crystallinity. The X-ray pattern is depicted in Figure 3.5. It was observed that growth in [110] direction starts diminishing in 50% F-TEDA sample. Further, it was observed that there is emergence of newer peak and significant changes in existing peaks. This may be attributed to change in phase of hematite and impurity. Therefore, the photo electrochemical study was carried out for pristine α-Fe_2O_3 and up to 40%wt. F-TEDA mediated F- α-Fe_2O_3.

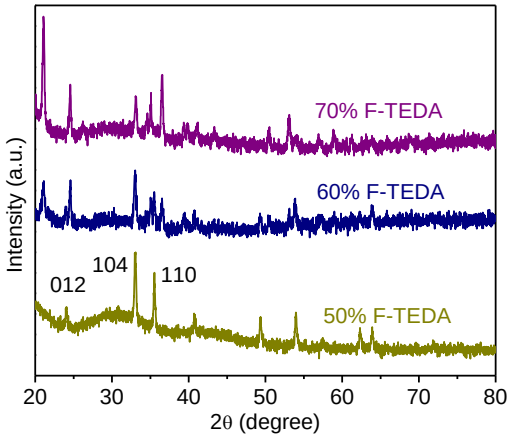

Figure 3.5: (a) XRD patterns of fluorinated hematite with respect to weight% (50%, 60% and 70%) of F-TEDA

3.2.5 XPS Analysis

In order to confirm the presence of fluorine, a detailed XPS analysis of pristine and F-Fe_2O_3 was performed. The XPS full range survey scan show signals corresponding to Fe 2p and Fe 3s, O 1s and C 1s along with an additional low count signal for F 1s in F-Fe_2O_3 (Figure 3.6).

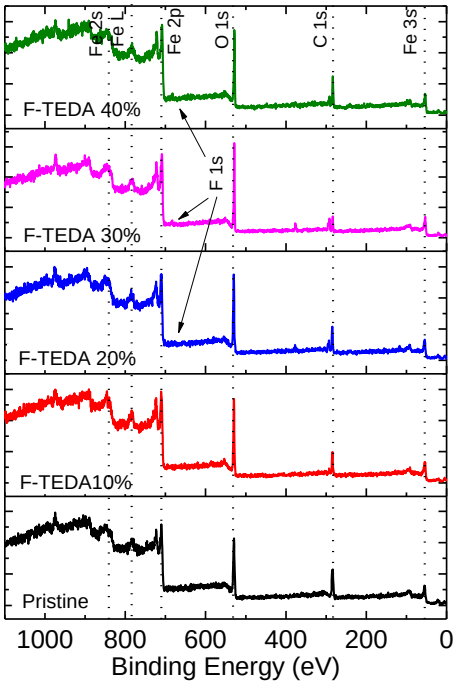

Figure 3.6: XPS full range survey scan of pristine α-Fe_2O_3 and F- α-Fe_2O_3

Upon fluorination, a downward shift in BE values was observed for Fe 2p and O 1s signals successively in all cases (Figure 3.7a and b) due to changes in the chemical state upon fluorine binding.[Zhu et al., 2013] Pristine Fe_2O_3 shows a doublet peak, with an energy split of ~13.5 eV, at ~723.1 eV and 709.6 eV that correspond to Fe $2p_{1/2}$ and Fe $2p_{3/2}$ respectively. The doublet peak values are consistent with the reported value of Fe^{+3} in pristine α-Fe_2O_3.[Karthikeyan et al., 2014] Fe $2p_{1/2}$ and Fe $2p_{3/2}$ signals in F-Fe_2O_3 (10-40%) are marginally shifted with increasing fluorine content (Table 3.2).

Table 3.2: Elemental quantification of Fe, O and F in pristine and F-Fe_2O_3. The peak values are calibrated with reference to adventitious carbon at 284.8 eV

F-TEDA (%)	Fe 2p		O 1s		F 1s	
	BE (eV)	At%	BE (eV)	At%	BE (eV)	At%
0	709.66	33.57	529.67	66.43	ND	0
10	709.58	33.57	529.63	66.43	ND	0
20	709.21	33.35	529.44	66.24	683.59	0.41
30	709.2	32.94	529.11	65.85	683.95	1.21
40	709.21	32.94	529.08	65.93	683.62	1.13

Pristine α-Fe_2O_3, upon de-convolution of O 1s, shows two peaks at 532.1 eV and 529.6 eV corresponding to surface hydroxide and lattice oxide respectively (Figure 3.7b) [Annamalai et al., 2016]. F-Fe_2O_3 (10-40%) exhibit prominent O 1s surface hydroxide signals that may be attributed to favorable formation of surface hydroxides due to fluorination. The core-level F 1s signal is weak and could not be noticed in 10 wt% F-TEDA however a broad and tiny peak appeared at ~ 683 eV for 20% and higher wt% of F-Fe_2O_3, thus confirming surface fluorination of Fe_2O_3 (Figure 3.7c). The quantitative estimation of fluorine shows 0.41 atomic %, 1.21 atomic % and 1.13 atomic % of fluorine for Fe_2O_3 synthesized with 20%, 30% and 40% weight of F-TEDA respectively (Table 3.2).

As per literature information (Table 3.3), the F 1s signal due to surface binding occurs at lower BE values (~684 eV) while doping of fluorine in solid solution results in BE shift at higher values (~688 eV) [Yu et al., 2002].

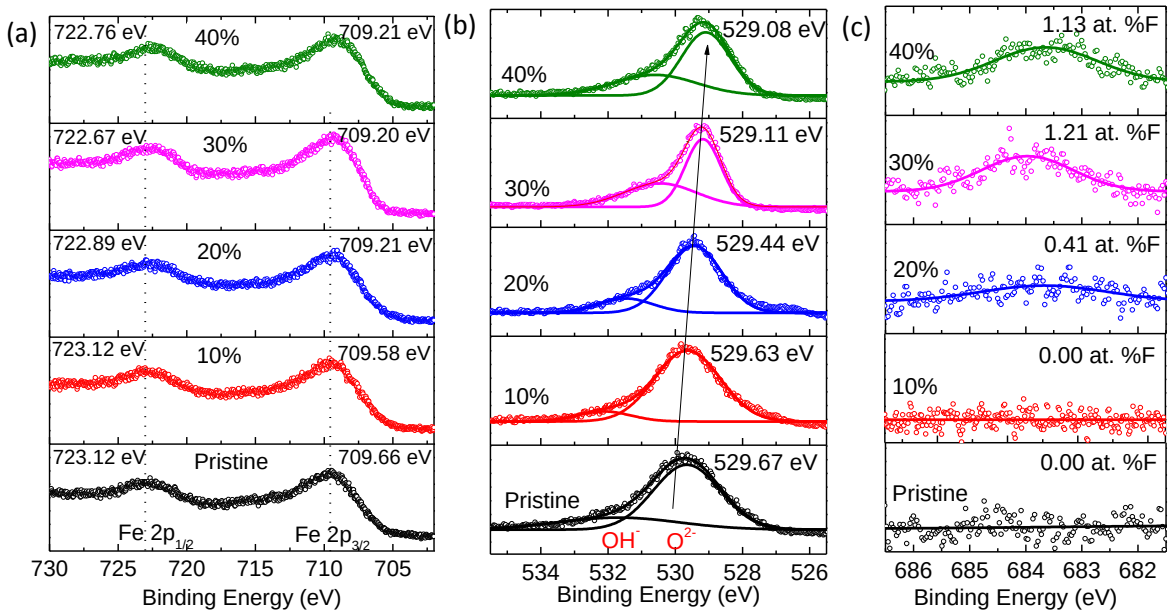

Figure 3.7: X-ray photoelectron spectra (XPS) of (a) Fe2p (b) O1s and (c) F1s of pristine α-Fe_2O_3 and F-Fe_2O_3. Note that the peak values are calibrated with reference to carbon at 284.8 eV

Interestingly, the peak at ~ 683 eV indicates the possibility of surface fluorination by fluoride formation and hydroxide ligand exchange at surface [Park and Choi, 2004],[Karthikeyan et al., 2014]. Since there is no F 1s signal at ~ 688 eV, the fluoride doping in solid solution was not accounted in this study. Therefore, F-TEDA introduces fluorine in α-Fe_2O_3 at the surface by replacing surface hydroxides. However, there is no evidence of replacing oxygen from its lattice.

Table 3.3: X-ray photoelectron spectra (XPS) literature reference of Fe 2p, O 1s and F 1s peaks.

S. No.	B.E. of Fe 2p (eV)		B.E. of O 1s (eV)			B.E. of F 1s (eV)	Comments	Reference
	$2p_{3/2}$	$2p_{1/2}$	OH^-	O^{2-}	H_2O			
1.	711.1	724.2	N.A	529.9	N.A	683	N.A	[Karthikeyan et al., 2014]
2.	710.3	723.7	N.A	N.A	N.A	683.8	BE is of F lower than F compounds due to doping	[Wang et al., 2017]
3.	711.2	724.2	531.7	530.2	N.A	N.A	N.A	[Annamalai et al., 2016]
4.	711.2	724.8	Main Peak of O 1s 530.2			686	F at 686 due to F adsorbed on surface and in the lattice. The BE of fluorinated γ-Fe_2O_3 samples is lower than that of pure γ-Fe_2O_3 samples, suggesting that the local chemical state was influenced by doping with F	[Zhu et al., 2013]
5.	N.A	N.A	N.A	N. A.	N. A.	684.3	The F 1s peak is originated from the surface fluoride (Ti-F) formed by ligand exchange between F^- and surface hydroxyl group on TiO_2	[Park and Choi, 2004]
6.	N.A	N.A	531 eV			684.8 and 688.6	Peak at 684.8 eV is due to F^- ions physically adsorbed on the surface of TiO_2. Peak at 688.6 eV is due to F in solid solution $TiO_{2-x}F_x$.	[Yu et al., 2002]
7.	N. A.	N. A.	~532.4	~529.1 and ~530.8	~533.6	N. A.	~529.1 eV is attributed to O^{2-} ions ~530.8 eV is oxidized metal ions in the lattice	[Ameen et al., 2012]
8.	N. A.	N. A.	532.1 and 531.3	530.4	533	N. A.	N. A.	[Knut et al., 2015]
9.	N. A.	N. A.	N. A.	N. A.	533.7	N. A.	N. A.	[Kunat et al., 2003]
10.	N. A.	N. A.	531.5	530.2	532.5	N. A.	N. A.	[Sepulveda-Guzman et al., 2009]
11.	N. A.	N. A.	531.1	529.7	532.6	N. A.	N. A.	[Bai et al., 2011]
12.	711.2	724.4	531.7	530.2	533.1	N. A.	N. A.	[Kim et al., 2014]

N.A.: Not applicable as data not provided.

3.2.6 Raman Spectra

The Raman spectra of α-Fe_2O_3 and F- α-Fe_2O_3 are displayed in Figure 3.8. The spectra of powder sample exhibit six prominent lines at about 224 cm^- (A_{1g}), 242 cm^- (E_g), 291 (E_g), 409 cm^- (E_g), 501 cm^- (A_{1g}) and 616 cm^- (E_g) which are typical for α-Fe_2O_3 crystal [Chamritski and Burns,

2005; de Faria et al., 1997; Massey et al., 1990]. The lines at 224 cm-, 242 cm-, and 291 cm- are associated with movement of iron ions. The position and peak width are almost remaining unchanged after fluorination which indicates similar crystallite size of α-Fe_2O_3 and F- α-Fe_2O_3. The fact was also observed in X-ray diffraction (Table 3.1). The symmetric breathing mode of O atom relative to each cation in the plane perpendicular to the crystallographic c axis was observed as E_g line at 409 cm-[Beattie and Gilson, 1970]. The intensity of 409 cm- line is decreasing with respect to F-TEDA in reaction medium. This may be attributed to preferential growth in one direction. XRD also revealed the favored growth in 110 planes. The appearance of LO line near 656 cm- peak indicates the lattice disorder which might have introduced during the crystallization of α-Fe_2O_3 in F-TEDA reaction mediated fluorination in hydrothermal reaction vessel [Chernyshova et al., 2007].

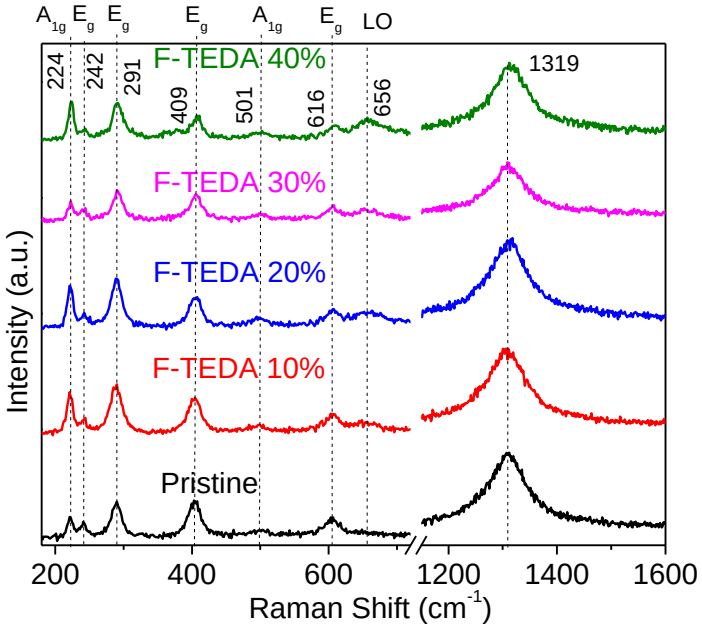

Figure 3.8: Raman spectra (XPS) of pristine α-Fe_2O_3 and F-Fe_2O_3

3.3 OPTICAL CHARACTERIZATION OF SURFCE FLUORINATED HEMATITE

The optical characterization of hematite and surface fluorinated hematite was carried out to obtain the information on any change in bandgap due to fluorination. The optical characterization was done by measuring UV Vis spectra and followed by bandgap calculation. These characterization data and their analysis are presented in sub-sections from 3.3.1 to 3.3.2 as following:

(3.3.1) *UV Visible diffused reflectance spectra.*
(3.3.2) *Tauc plot* for bandgap measurement.

3.3.1 UV Visible Diffused Reflectance Spectra

In order to elucidate the effect of surface fluorination on optical properties of α-Fe_2O_3, the UV-Vis diffused reflectance spectra are recorded for pristine and F-Fe_2O_3. The powder sample was placed in sample holder and measurement was done with reference to PTFE.

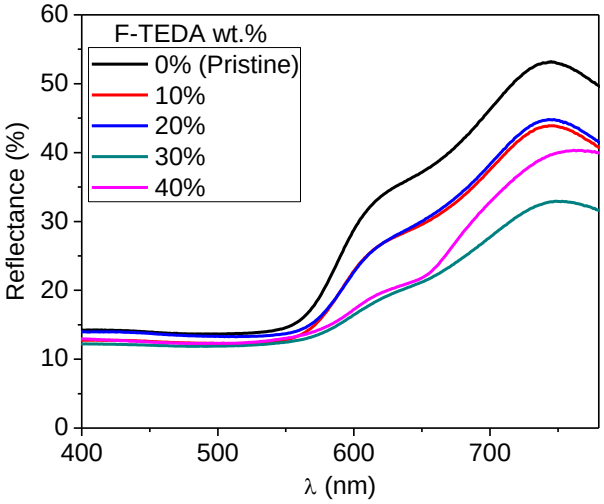

Figure 3.9: UV-Vis diffuse reflectance spectra

The diffused reflectance spectra are presented in Figure 3.9. There is marked changes in the %reflectance of pristine and fluorinated α-Fe_2O_3. The diffused reflectance data were further used for bandgap calculation.

3.3.2 Bandgap Calculation

The obtained reflectance data were converted to modified Kubelka–Munk (K-M) function using following equation:

$$F = \frac{(1-R)^2}{2R} \qquad (3.3)$$

The modified Kubelka–Munk function was plotted using Tauc equation. The band edge in Tauc plot was extrapolated to the *x*-axis for obtaining the bandgap of pristine and F-Fe_2O_3 samples. The Tauc plot and bandgap are presented in Figure 3.10.

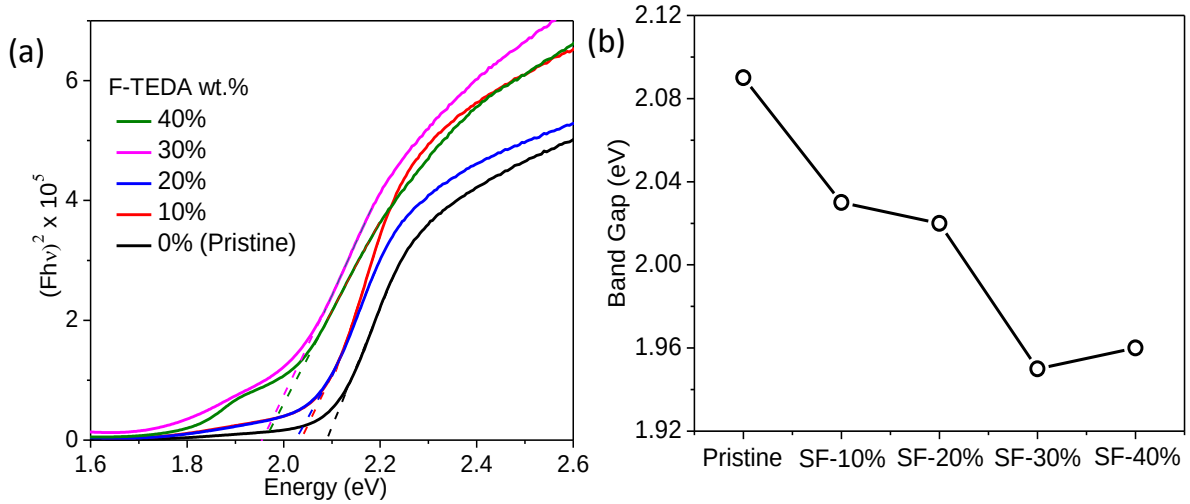

Figure 3.10: (a) Tauc plots of pristine and F-Fe_2O_3 (b) Variation in bandgap values of α-Fe_2O_3 upon fluorination

It can be seen that bandgap of F-Fe_2O_3 gradually decreases as compared to pristine α-Fe_2O_3 (Figure 3.10b) which is in agreement with their lower reflectance in Figure 3.9. This may be attributed to improved surface electrical conductivity of F-Fe_2O_3. The direct bandgap measured for pristine α-Fe_2O_3 (2.09 eV) matches well with literature bandgap values 2.0–2.2 eV. This optical absorption in the visible spectrum demonstrated that F-Fe_2O_3 has immense potential as photo-anode material due to possibility of tailoring the bandgap with changing in the concentration of F-TEDA. Since, an ideal photo-anode requires suitable bandgap large enough (>1.6 eV) to split water and faster electron transport and small enough (2.2 eV) to

absorb a wide range of the solar spectrum. F-Fe_2O_3 was further tested for electrochemical properties.

3.4 ELECTROCHEMICAL CHARACTERIZATION

The electrochemical characterization of hematite and surface fluorinated hematite was performed to get the information about photo current density, current sustainability and position of valance band & conduction band. The hydrogen generation experiments were also performed. DSSC cell was fabricated to see the fluorination effect. These characterization data and their analysis are presented in sub-sections from 3.3.1 to 3.3.4 as following:

(3.4.1) *J-V characterization and amperometry experiments*
(3.4.2) *Impedance spectroscopy (EIS) analysis*
(3.4.3) *Fluorination impact on dye sensitized solar cell (DSSC)*

3.4.1 J-V Characterization

α-Fe_2O_3 films were prepared on FTO glass slides over 2 cm^2 area by screen printing. Three consecutive layers of α-Fe_2O_3 was deposited to get the optimized thickness of ~10 µm. Films were annealed at temperature of ~500 °C. Further, electrodes were prepared using copper foil, silver paste and purified coal tar. The prepared working electrodes are presented in Figure 3.11a. Three electrode system was prepared using Ag wire as counter electrode and Ag/AgCl as reference electrode and it is presented in Figure 3.11b. The photo-electrochemical measurements of the α-Fe_2O_3 films were performed in 1.0 M aqueous KOH solution (pH = 13.6) under 100 W/m^2 light illumination, as shown in Figure 3.11c.

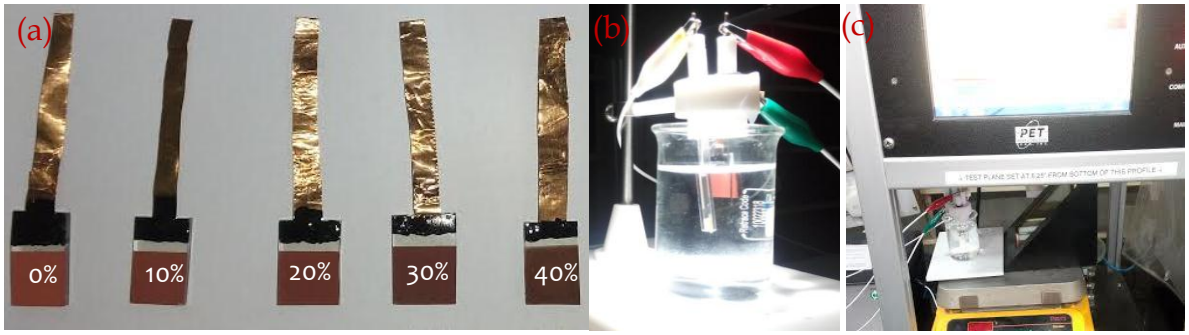

Figure 3.11: (a) Working electrode of pristine and F-Fe_2O_3 (with increasing F-TEDA concentration) and (b) Three electrode system (c) photo-electrochemical measurement setup

Based on the optical properties and X-ray patterns, F-α-Fe_2O_3 with preferred (110) orientation is expected to show a higher photo-electrochemical activity compared to pristine α-Fe_2O_3. As expected, the current density is almost negligible for pristine α-Fe_2O_3 as shown in Figure 3.12a. Current density increases with increasing fluorine content in α-Fe_2O_3. The trend continued till 30% F-TEDA sample and current density reaches maximum value of approximately 4 µAcm^{-2}. The current density value decreases at 40% F-TEDA sample due to lower atomic % of F atoms as seen from the XPS analysis The increase in photocurrent at higher at.% of F may be attributed to the fact that F atoms generate charge imbalances at Fe_2O_3 surface resulting in a slower recombination of the electron-hole pairs.[Zhu et al., 2013] Therefore, the electron and holes are available at surface and have the better opportunity to react with water. In addition to this the favorable (110) orientation has also helped for better charge collection at surface.

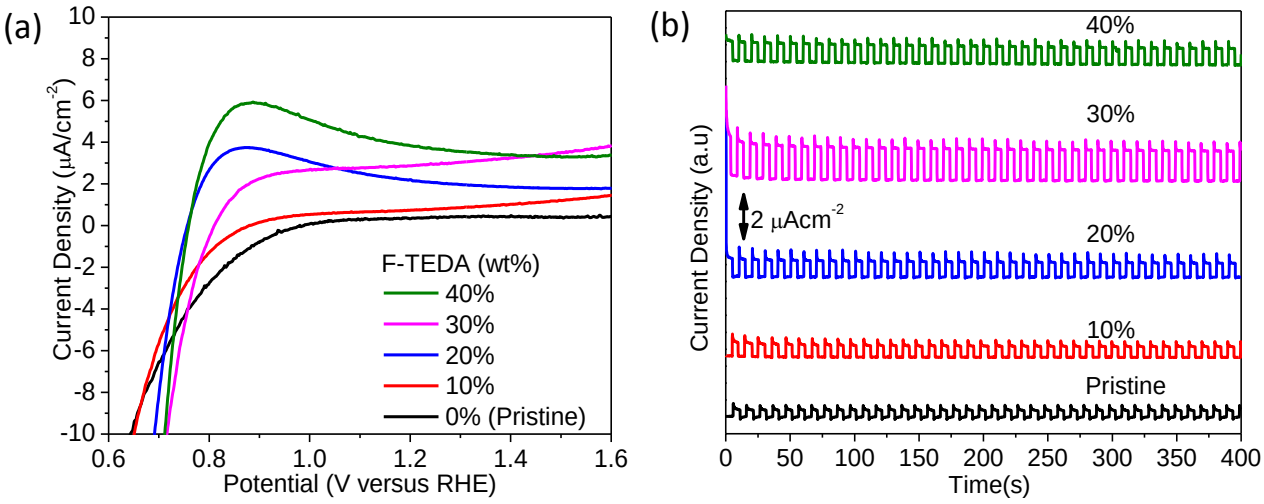

Figure 3.12: (a) J-V characteristics of α-Fe_2O_3 films in light (100 W/m2). (b) Chronoamperometry measurements performed at 1.6 V versus RHE.

Amperometry response was also recorded to investigate the stability of photo current. Figure 3.12b shows an amperometric (I-T) curve under applied voltage bias of 1.6 V vs RHE or 1 V vs Ag/AgCl for 400 seconds continuously under 100 W/m^2 illumination conditions. Current density was measured with light on and off interval of 5 s. The stability of the photo- current density throughout the measurement period demonstrates the potential of F-α-Fe_2O_3 as a photo anode.

The schematic of improved performance of F-α-Fe_2O_3 is presented in Figure 3.13, indicating that the surface fluorination reduces recombination & hence improving PEC performance.

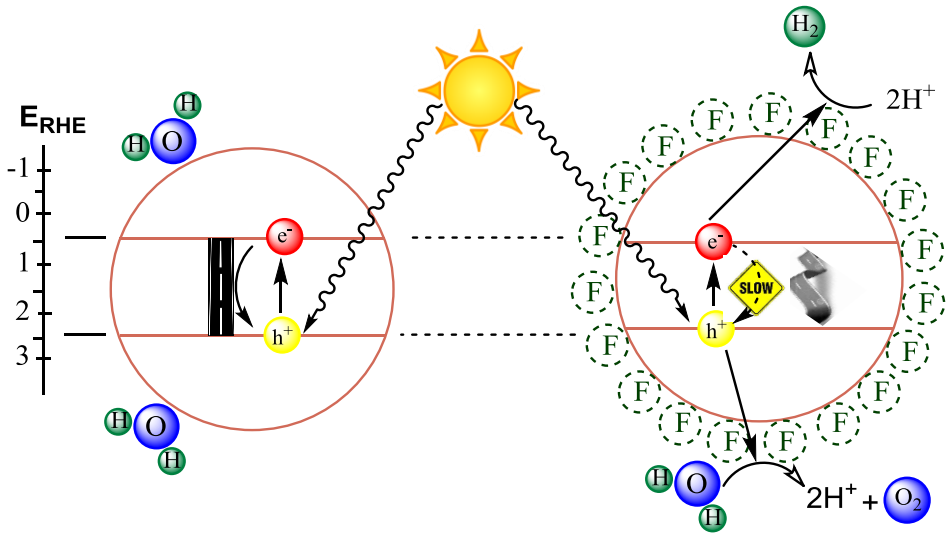

Figure 3.13: Impact of fluorination on electron hole recombination and better charge transport at surface

Figure 3.14a shows the photocurrent response of hematite and fluorinated hematite in the interval of 5 seconds. It is evident from figure that 30% F-TEDA samples exhibits the maximum current density. Hematite and fluorinated hematite samples exhibited characteristic *spike and overshoot* photocurrent transient upon chopped illumination. The spike is observed due to instantaneous photocurrent generated by swift movement of electrons and holes towards the semiconductor electrolyte junction [Dunn et al., 2014]. At this junction some of the holes participate in oxidation of water to molecular oxygen and many of the holes undergoes

recombination. Hole transfer efficiency (η_{trans}) is one of the important parameter for a photo catalytic material. It is the ratio of steady state photocurrent to instantaneous photocurrent, $\frac{J_{SS}}{J_{(t=0)}}$. The flux of holes that are transferred successfully to the electrolyte without undergoing recombination with electrons generates steady state photo current. Therefore, the instantaneous photocurrent signifies charge separation efficiency. However, the transfer efficiency is actual measure of available holes for water splitting.

It is observed that the instantaneous photocurrent increase with increased surface fluorination. This effect is observed till 30% F-TEDA. However, the transfer efficiency increases till 40% F-TEDA.

The photo current response of fluorinated films were plotted with respect to pristine Fe_2O_3 films. Surface fluorination shows significant enhancement in photo current. The 10% F-TEDA sample shows 100% change whereas 30% sample shows 350% increment in photocurrent. (Figure 3.14b) Further addition of F-TEDA in the reaction mixture results in lowering of photo current. Therefore 30% F-TEDA was found to optimum for getting maximum photo current and incorporation of highest amount of fluorine in Fe_2O_3.

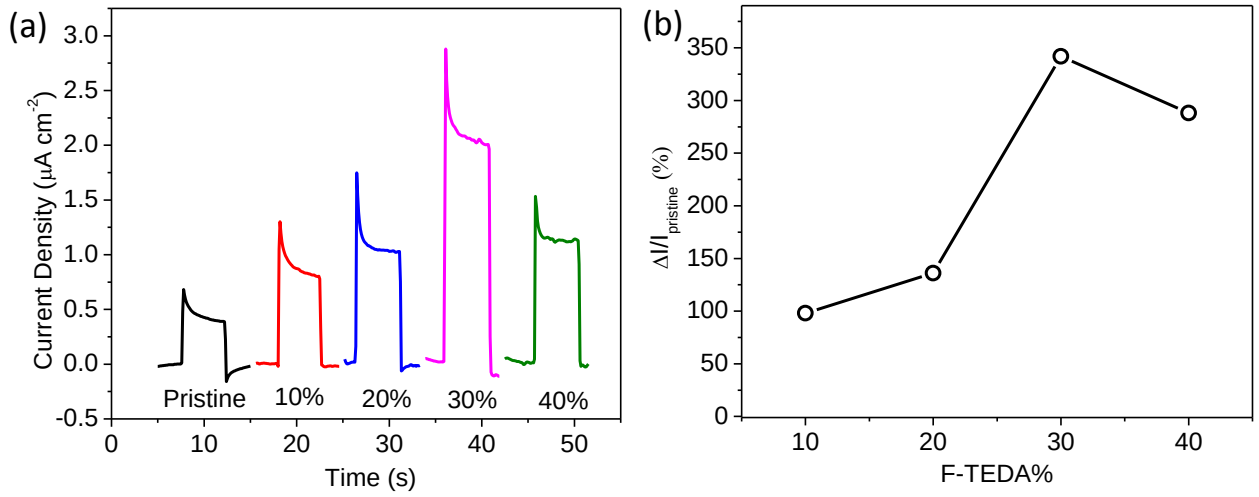

Figure 3.14: (a) I-t curve of pristine and fluorinated Fe_2O_3 films on exposure to light for 5 s. (b) The photocurrent response with respect to pristine Fe_2O_3 films

Effect of different layer thickness on current density was studied for F-Fe_2O_3 (Figure 3.15a). Amperometric measurements exhibit a successive increment in the current density with increased thickness of the film. Increase in thickness beyond three layers, lead to peeling off the film from the FTO substrate during measurements. Thus, all experiments were performed using three layer deposited by screen printing on FTO glass as substrate.

To find the optimum calcination temperature, fluorinated α-Fe_2O_3 (10% F-TEDA sample) was calcined at 500 °C and 700 °C. Better current density was observed at 500 °C. Therefore, the screen printed films were calcined at 500 °C for study (Figure 3.15b).

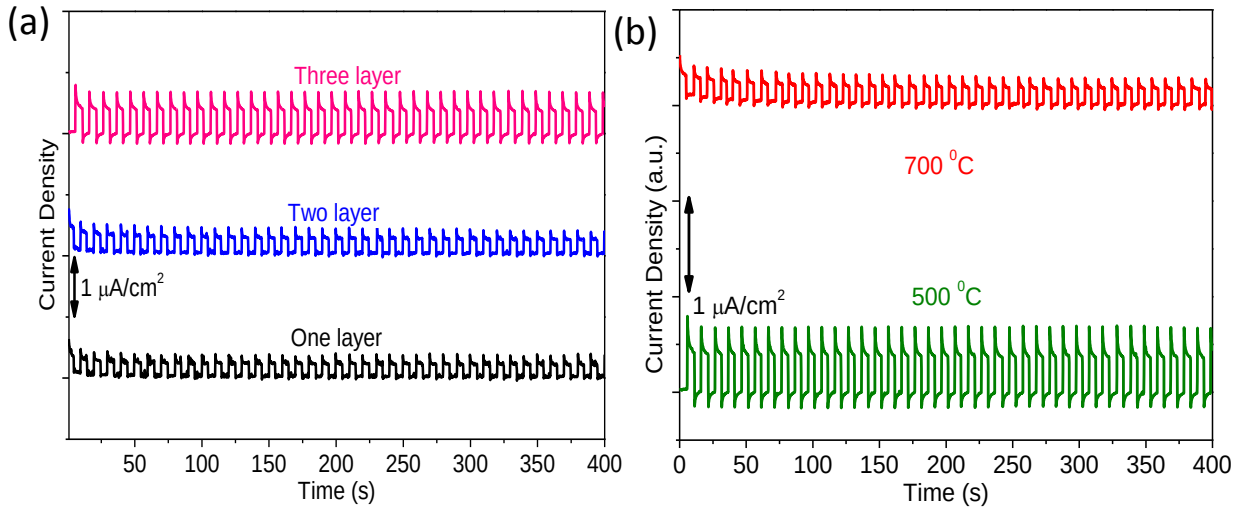

Figure 3.15: (a) Amperometric measurements at 1.6 V versus RHE of different thicknesses (b) Current density of fluorinated α-Fe_2O_3 at different calcination temperature prepared by screen printing (F-TEDA 10% wt.)

3.4.2 Impedance Spectroscopy (EIS) Analysis

The flat band potential and donor densities of films were calculated from the Mott–Schottky plot (Figure 3.16a). The Mott–Schottky plots were extrapolated to the x-axis to calculate the respective conduction band edge in all cases.

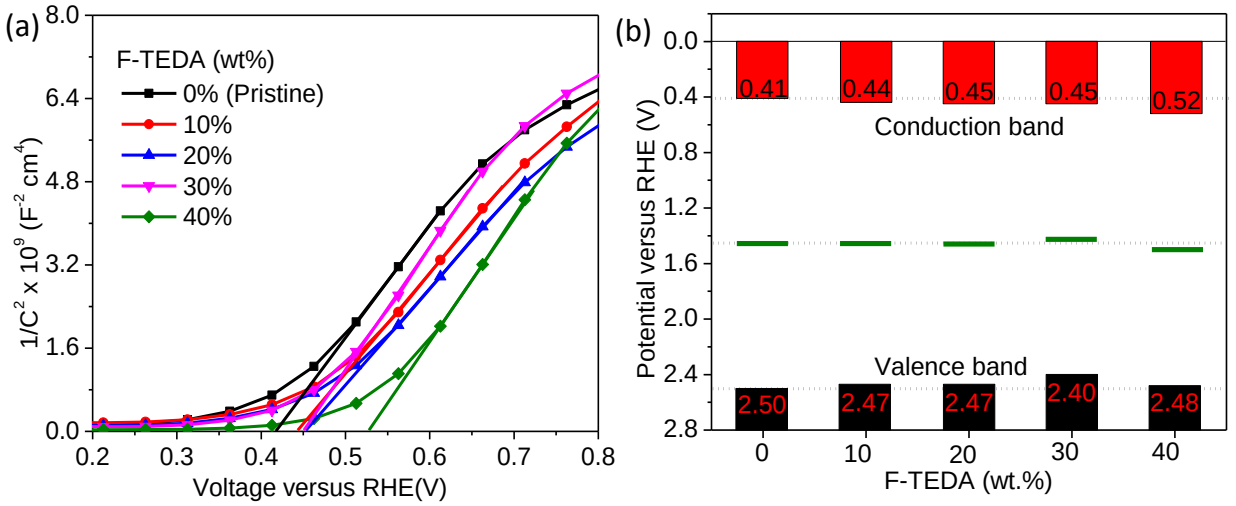

Figure 3.16: (a) Mott–Schottky plots of pristine Fe_2O_3 and F-Fe_2O_3. The intercept of the linear extrapolation with the x-axis (potential) marks the flat band potential as $(U_{fb} + \frac{K_b T}{e})$. (b) Band structure of the synthesized Fe_2O_3 with different quantity of F-TEDA. Conduction band (red bars), the approximate position of the mid-bandgap energy level (green line), and the valence band (black bars)

Pristine α-Fe_2O_3 yielded a conduction band edge of 0.41 V versus RHE, in agreement with previously reported values [Bassi et al., 2014]. The valence band position was also calculated by adding the value of bandgap, obtained from diffused reflectance measurements, to conduction band edge. The band structure consisting of the conduction band, the approximate position of the mid-bandgap energy level, and the valence band of pristine and F-α-Fe_2O_3 are shown in Figure 3.16b. The effect of surface fluorination is clearly visible from the shift observed in the conduction band edge from 0.41 V (pristine) to 0.52 V versus RHE of F-Fe_2O_3 with higher wt% of F-TEDA. The lowering of conduction band level (positive position) and increase in photocurrent density may be attributed to increase in surface charge density upon fluorination. The carrier densities (N_d) calculated from slopes of Mott–Schottky plots of

the doped samples are within the same order of magnitude (~10^{19}) including pristine α-Fe_2O_3 (Table 3.4). The surface fluorine is not an actual dopant however its surface attachment contributes to lowering of flat-band potential.

Table 3.4: Charge carrier densities calculated from Mott Schottky plot

SNo	%F-TEDA	$N_d(cm^{-3})$
1.	0	8.49×10^{19}
2.	10	9.14×10^{19}
3.	20	9.28×10^{19}
4.	30	7.48×10^{19}
5.	40	7.34×10^{19}

Electrochemical impedance spectroscopy (EIS) measurements of pristine and F-Fe_2O_3 are shown in Figure 3.17. This gives the information about variety of conductivity. The representative Nyquist plots were plotted from a frequency range of 1–10^5 Hz and fitted to a 2-RC-circuit model which consists of the resistance of FTO, R_s, the charge transport resistance in the bulk, R_{CT1}, charge transfer resistance at the hematite/ electrolyte interface, R_{CT2}, the space-charge capacitance of the bulk hematite, CPE_1 and the Helmholtz capacitance at the hematite/electrolyte interface, CPE_2.

The calculated equivalent circuit parameters by fitting according to the equivalent circuits are shown in Table 3.5. It can be observed that all fluorinated hematite samples shows reduced charge transport resistance in the bulk in comparison with the bare hematite along with an increase in the resistance at the hematite/ electrolyte interface upon fluorination.

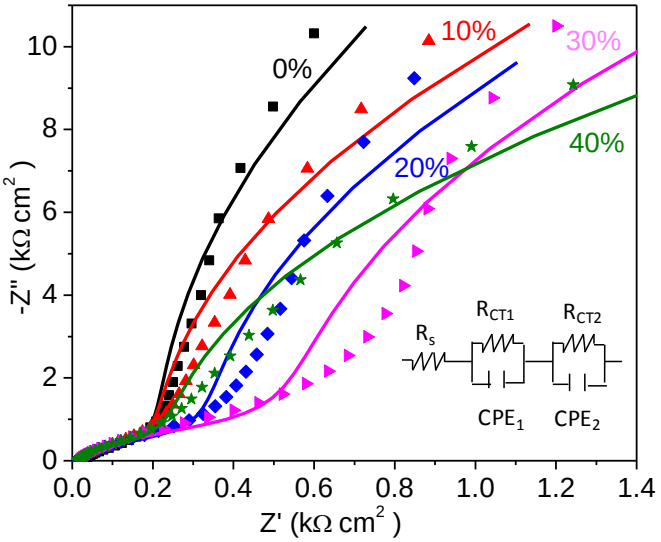

Figure 3.17: Nyquist plot of pristine and F- F-Fe_2O_3 (10-40% F-TEDA) of electrodes in photo-electrochemical cell in 3- electrode geometry

Table 3.5: Fitting parameters from Nyquist plot of pristine and F-Fe_2O_3 films

S. No.	%F-TEDA	E_{fb} (V)	R_s ($\Omega\ cm^2$)	R_{CT1} ($k\Omega\ cm^2$)	CPE ($\mu F\ cm^{-2}$)	R_{CT2_1} ($\Omega\ cm^2$)	CPE_2 ($\mu F\ cm^{-2}$)
1.	0	0.41	18.78	213	15.14	184	24.08
2.	10	0.44	13.37	203	14.97	197	21.10
3.	20	0.45	12.39	120	18.43	329	16.40
4.	30	0.45	17.89	116	14.32	433	14.14
5.	40	0.52	13.79	68	16.53	226	23.92

3.4.3 Fluorination Impact on Dye Sensitized Solar Cell (DSSC)

α-Fe_2O_3 has been used as photo-anode as well as counter-electrode in dye sensitized solar cells [Shahpari et al., 2015; Yang et al., 2016]. α-Fe_2O_3 as photo anode is not much explored due to its poor charge carrier mobility.[Sivula et al., 2011] DSSCs were fabricated using different fractions of F-Fe_2O_3 (F-TEDA-20%) and pristine Fe_2O_3 with TiO_2 as photo anode material for optimized performance (Figure 3.18).

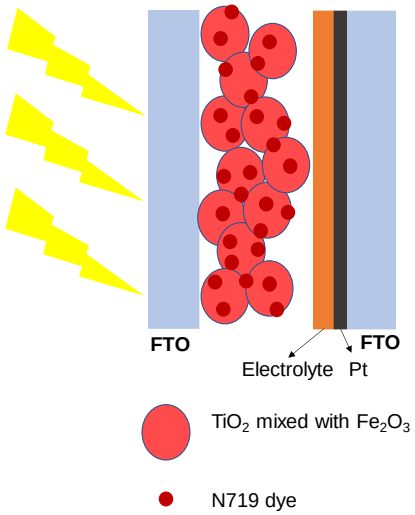

Figure 3.18: Schematic representation of dye sensitized solar cells fabricated using α-Fe_2O_3/TiO_2 as photoanode

DSSC fabrication: All solar cells were prepared according to the typical method as described in previous study [Shejale et al., 2016]. Briefly, pristine and F- Fe_2O_3 (30%) were mixed with TiO_2 (P25) powders in 5:95, 10:90, 20:80 and 40:60 ratios in the form of a paste and uniformly grinded with ethyl cellulose in ethanol and α-terpinol (wt % ratio: 2.7:3.38:1). The paste was screen printed on the fluorine doped tin oxide (FTO) substrates and dried for 6 min at 120 °C. It is repeatedly printed 4-5 times to increase the thickness of layer. Material film of ~ 15 µm thickness on FTO is obtained after the sintering of electrode at 450 °C for 30 min in the air. The counter electrode is prepared by depositing platinum sol onto the FTO and followed by calcined at 450 °C for 30 min. Further, photo anodes were dipped for 18 hrs in 0.5 mM N719 dye solution. Finally, the sandwich structured DSSC is obtained by assembling soaked photoanodes and Pt counter electrode using Iodolyte Z 50 (Solaronix) as the electrolyte and a Surlyn spacer as shown in Figure 3.18. The fabricated DSSC device was then illuminated under solar simulator 1000 W/m^2 for J-V and EIS measurements. All the fabricated DSSCs were averaged over three cells. Eight different sets of DSSCs were fabricated for different combinations of photo anode and their photovoltaic parameters are given in Table 3.6.

Table 3.6: Photovoltaic performance parameters of the DSSC based on α-Fe_2O_3/TiO_2photoanode

Pristine α-Fe_2O_3					
Cell No.	*Fe_2O_3 (wt%)*	*J_{SC} (mA)*	*V_{OC} (V)*	*FF %*	*η (%)*
1	5	4.85±0.33	0.627±0.02	68±1.73	2.09 ± 0.27
2	10	6.04±0.49	0.667±0.02	70±1	2.83±0.13
3	20	3.40±0.24	0.621±0.01	61.9±8.79	1.32±0.29
4	40	2.84±0.16	0.587±0.023	46.33±0.58	0.77±0.08
F-Fe_2O_3 (20%)					
5	5	6.023±0.35	0.675±0.01	63.33 ± 2.51	2.58±0.10

6	10	7.24±0.14	0.678±0.01	67	3.31±0.11
7	20	2.93±0.167	0.547±0.18	57.67±5.78	1.09±0.04
8	40	2.11±0.16	0.646±0.01	65±3.6	0.89±0.06

The photocurrent density versus voltage (J-V) curves of the DSSCs fabricated with various proportions of pristine and F-Fe_2O_3 with TiO_2 (5:95, 10:90, 20:80 and 40:60) respectively is presented in Figure 3.19a and 3.19b. DSSCs fabricated from pristine and F-Fe_2O_3:TiO_2 of 10:90 ratio exhibit maximum power conversion efficiency, η of 3.41% and 2.75 % beyond which it decreases probably due to higher reflectance from F-Fe_2O_3 (Figure 3.19c). The power conversion efficiency η (%) in case of F-Fe_2O_3 : TiO_2 (10:90) was higher than pristine Fe_2O_3 mixture by 16% probably due to higher dye intake in F-Fe_2O_3 due to modified surface properties despite of decrease in BET surface area of pristine α-Fe_2O_3 upon fluorination (41.2 m^2/g for pristine while 5.0 m^2/g for α-Fe_2O_3 with 20% F-TEDA concentration). However, there was not much influence on the pore radius (from 28.7 Å to 27.7 Å).

The photovoltaic parameters including the current density (J_{SC}), voltage (V_{OC}), fill factor (FF) and power conversion efficiency (η) of this study have been summarized in Table 3.6. To study the charge-transfer process taking place at the interface, EIS spectra of DSSC fabricated using pristine hematite and fluorinated hematite are shown in Figure 3.19d.

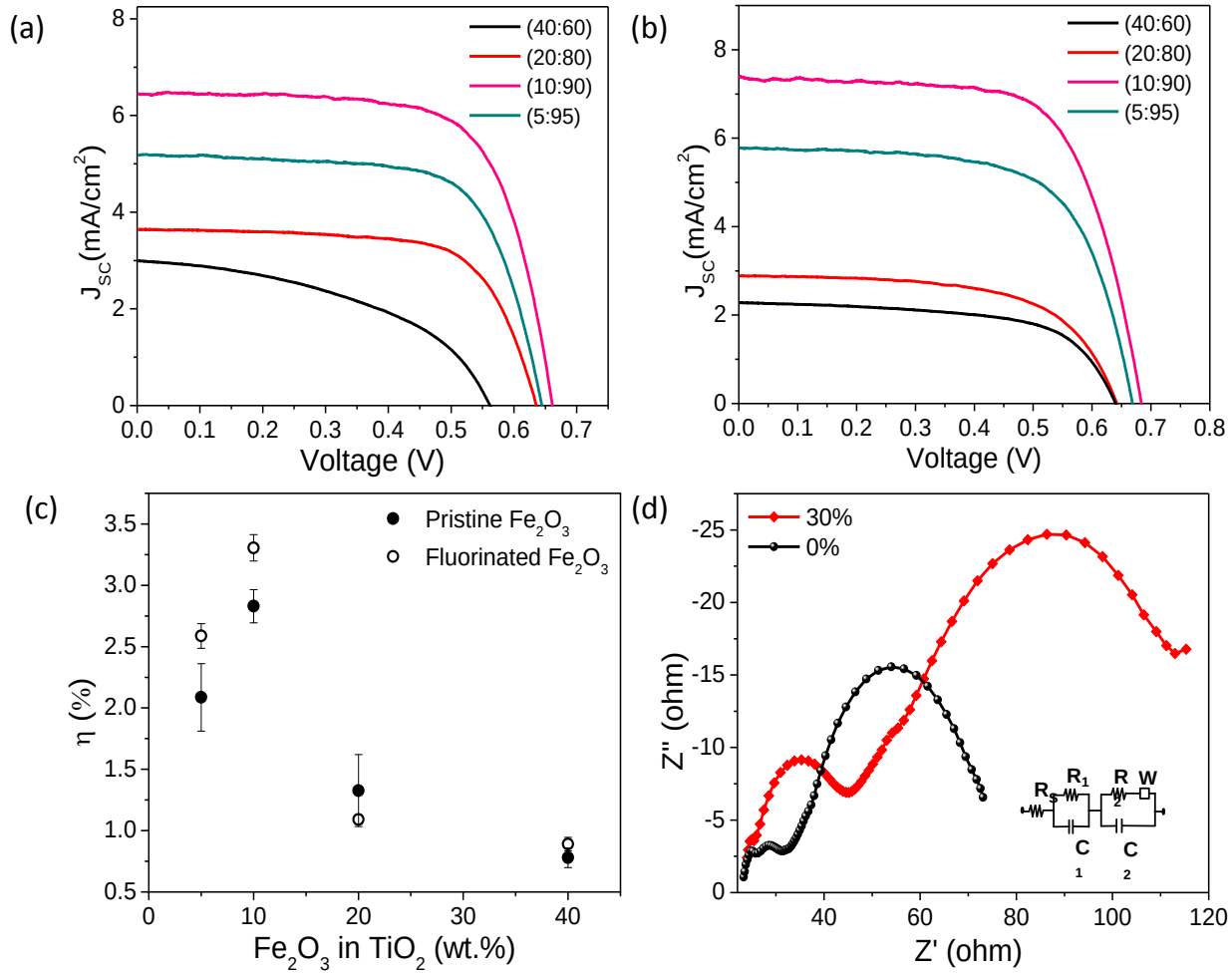

Figure 3.19: J-V characteristics of (a) pristine α-Fe2O3 and (b) 30% F-Fe2O3 photo anode mixed in different weight ratios with TiO2 (P25) as photo anode. (c) Photo-conversion efficiency (d) Nyquist plot of the optimized composition (10% of Fe2O3 in TiO2) for pristine and F-Fe2O3respectively. Inset shows an equivalent circuit diagram

Well defined semicircles representing the charge transfer resistance occurring between the Pt counter electrode and the redox electrolyte (I^-/I_3^-) system were observed in the high frequency region for pristine and F-Fe_2O_3 photo anodes based DSSCs. The charge transfer resistance is higher in case of F-Fe_2O_3 compared to pristine and thus it can be inferred that the former has a lower recombination rate. Furthermore, the electron lifetime, τ_n was calculated to be 0.074 ms and 0.044 ms ($\tau_n = R_1 \times C_1$) for pristine and F-Fe_2O_3 respectively (Table 3.7)

Table 3.7: Parameters obtained by fitting equivalent circuit diagram using Nyquist plot for DSSC

S. No.	*Photo anode for DSSC*	R_S (Ω)	R_1 (Ω)	C_1 (μF)	$\tau_n=(R_1 \times C_1)$ (ms)
1	Pristine α-Fe_2O_3	24.45	27.94	2.655	0.074
2	Fluorinated α-Fe_2O_3 (20%)	33.62	35.96	1.654	0.059

3.5 CONCLUSION

F-Fe_2O_3 nanostructures were synthesized via a facile hydrothermal route using Selectfluor (F-TEDA) as a fluorinating as well as growth directing agent. The addition of successive amount of F-TEDA to Fe precursor under hydrothermal conditions resulted in preferential growth of α-Fe_2O_3 along (110) orientation suppressing the commonly observed (104) direction by ~ 35%, the former being important for enhanced charge transport. With increasing fluorination, the hierarchical dendritic-type α-Fe_2O_3 converts to a snow-flake type structure (F-TEDA-20%) anisotropically growing along the six directions and at higher F-TEDA concentrations (above 30%), loosely held particulate aggregates get formed. The extent of fluorination was highest of 1.21 atomic % with 30% F-TEDA and it was supported by X-Ray Photoelectron Spectroscopy (XPS) measurements. Due to fluorination, optical absorption exhibited a reduction in optical bandgap from 2.10 eV in case of pristine to 1.95 eV for F-Fe_2O_3. Screen-printed films of F-Fe_2O_3 in photo electrochemical cell exhibited an enhanced current density at illumination of ~100 W/m^2. Increase in photo electrochemical activities were attributed to the fluorination induced preferred growth along the (110) direction as well as surface fluorine atoms resulting in improved charge transfer efficiency and reduced recombination losses. As a photo anode material, 20% F-Fe_2O_3 was taken in an optimized ratio of 10:90 with respect to P25-TiO_2 showed improved performance in dye sensitized solar cells (DSSC) with an increase in efficiency by ~16%.